

Post-growth modulation doping by ion implantation

Cite as: Appl. Phys. Lett. **117**, 263502 (2020); doi: [10.1063/5.0031992](https://doi.org/10.1063/5.0031992)

Submitted: 5 October 2020 · Accepted: 13 December 2020 ·

Published Online: 28 December 2020



View Online



Export Citation



CrossMark

P.-Y. Chiu,¹ D. Lidsky,² Y. Chuang,¹ Y.-H. Su,¹ J.-Y. Li,^{1,3,4}  C. T. Harris,^{2,5}  and T. M. Lu^{2,5,a)} 

AFFILIATIONS

¹Graduate Institute of Electronic Engineering, National Taiwan University, Taipei 10617, Taiwan

²Sandia National Laboratories, Albuquerque, New Mexico 87185, USA

³Taiwan Semiconductor Research Institute, Hsinchu 30078, Taiwan

⁴Department of Electrical Engineering, National Taiwan University, Taipei 10617, Taiwan

⁵Center for Integrated Nanotechnologies, Sandia National Laboratories, Albuquerque, New Mexico 87123, USA

^{a)}Author to whom correspondence should be addressed: tlu@sandia.gov

ABSTRACT

Modulation doping is a commonly adopted technique to create two-dimensional (2D) electrons or holes in semiconductor heterostructures. One constraint, however, is that the intentional dopants required for modulation doping are controlled and incorporated during the growth of heterostructures. Using undoped strained germanium quantum wells as the model material system, we show, in this work, that modulation doping can be achieved post-growth of heterostructures by ion implantation and dopant-activation anneals. The carrier density is controlled *ex situ* by varying the ion fluence and implant energy, and an empirical calibration curve is obtained. While the mobility of the resulting 2D holes is lower than that in undoped heterostructure field-effect transistors built using the same material, the achievable carrier density is significantly higher. Potential applications of this modulation-doping technique are discussed.

Published under license by AIP Publishing. <https://doi.org/10.1063/5.0031992>

Two-dimensional (2D) electrons or holes have long served as an ideal model system for physicists to test out condensed matter theories and for engineers to build electronic and optical devices.¹ Some next-generation computing architectures, such as spintronics and quantum computing, also use 2D electrons or holes as the starting point.^{2–7} The more widely used approaches for generating 2D carriers in a host semiconductor heterostructure include the modulation-doping technique, field-effect transistor (FET) architecture, persistent photoconductivity, and polarization-induced carriers. Persistent photoconductivity, where carriers are generated by illumination,^{8–11} and polarization-induced carriers, which arise from the intrinsic polarization mismatch at interfaces in the host heterostructure,^{12–17} are typically highly material specific, as they rely on the existence of certain defect states in the material and certain crystal orientations of the host heterostructure. The FET architecture and modulation doping are generally considered more generic, material-agnostic approaches. In an FET, a metallic gate is separated from the active channel by a thin dielectric layer, and carriers are induced through capacitive coupling.¹ The silicon metal-oxide-semiconductor FET (MOSFET) being the most common, high-quality undoped heterostructure FETs (HFETs) have been demonstrated in several semiconductor systems, such as Si/

SiGe,^{18,19} GaAs,^{20–22} and Ge/GeSi.^{23–25} While the FET architecture is extremely versatile and is adapted for various applications across material platforms, it is by no means the answer to all needs, especially for applications at cryogenic temperatures. First of all, it is not trivial to obtain a high-quality dielectric/semiconductor interface except for bulk silicon because of thermal budget or intrinsic materials chemistry. A direct consequence is the difficulty in achieving high-yield fabrication of gated devices that do not show gate leakage. Non-ideal interfaces also manifest themselves in sometimes insurmountable stability and reliability problems. For silicon MOSFETs, the interface states and trapped charge located at the interface where the 2D carriers reside can impose a strong disorder potential. Architecturally, the existence of a strongly conducting metallic gate next to the 2D carriers significantly changes the dielectric environment, disorder landscape, and screening for the induced 2D carriers and can interfere with microwave and optical experiments. As such, needs for a technique that creates a simple, standalone 2D system remain for certain problems and applications. A built-in 2D system without the need for gating bypasses the gate leakage problem and typically shows better charge stability, as the charge distributions are closer to thermal equilibrium.

The modulation-doping technique, first applied to the GaAs/AlGaAs system^{26,27} and later transplanted to many other material systems,^{28–32} is the canonical approach to creating high-mobility 2D electrons or holes in semiconductor heterostructures without the need for gating. By placing dopants in the barrier layers flanking a quantum well, carriers from the intentional dopants transfer into the quantum well, creating a sheet of mobile carriers while leaving behind ionized dopant cores. Modulation doping is almost invariably implemented by supplying the required intentional dopants during the growth of heterostructures. In particular, dopants are typically introduced and incorporated into the structure when the target barrier layer is being epitaxially grown. Precise control of the doping density and location is of ultimate importance, as it determines the carrier density and mobility of the grown heterostructure. In practice, fine control of doping density at the sub-monolayer level is not trivial and is often not as precise as desired, resulting in variability from growth to growth. The dopant concentration is typically controlled by setting the temperature of the dopant source, which, in turn, sets the dopant flux in molecular beam epitaxy, or by varying the dopant gas flow rate in chemical vapor deposition, in addition to controlling the substrate temperature, which determines the dopant incorporation efficiency. As the temperature dependence of incorporation is typically exponential, slight variations in the source and substrate temperatures cause strong variations in the active dopant density. On the other hand, the doping density control in the implantation modulation-doping technique is achieved by controlling the implant fluence, which is achieved by measuring the ion beam current and implantation time. Such electrical measurements can be very accurate. The main uncertainty would arise from the annealing temperature, which affects the activation ratio. Since the physical upper bound would be 100% activation, the variation in doping density is tighter. Furthermore, the doping level in a grown heterostructure is set and hard to change after growth, while the implantation modulation-doping technique allows fine tuning of the doping type, depth, and density in a given heterostructure.

In this work, we present the concept of and demonstrate experimentally post-growth modulation doping using ion implantation and dopant-activation anneals. We used undoped Ge/GeSi heterostructures as a model material system.²³ We simulated the dopant profiles of implanted Ga ions using the Stopping and Range of Ions in Matter/Transport of Ions in Matter (SRIM/TRIM) package³³ and performed the simulated implantation to achieve modulation doping. After activating the implanted dopants through rapid thermal anneals, we characterized the samples using magneto-transport, and the densities and mobilities were extracted. We obtained an empirical relation between the active 2D hole density and the implantation fluence, which serves as a guide for post-growth tuning the 2D hole density. We observed that the mobility is degraded compared to that achieved in an undoped heterostructure FET (HFET) built using the same material, presumably due to implantation-induced damage. The achievable density, nevertheless, is higher than that in the HFET, highlighting the unique advantage of the implantation modulation-doping technique.

Figure 1 shows a schematic drawing of the structure of the starting material as well as supporting data from transmission electron microscopy (TEM), secondary ion mass spectroscopy (SIMS), and x-ray reciprocal space map (RSM). The cross-sectional TEM image and the SIMS profiles agree well and show a 19-nm-thick Ge quantum well buried under a 62-nm-thick GeSi undoped spacer. The SIMS

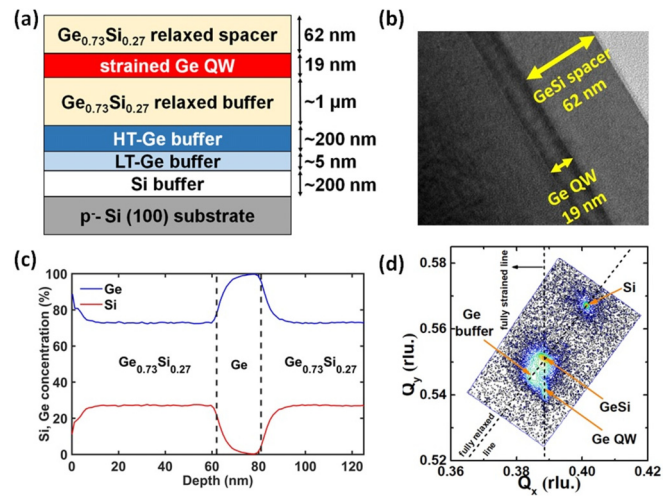


FIG. 1. (a) A schematic view of the cross section of the Ge/GeSi heterostructure used in this work. (b) A cross-sectional TEM image and (c) the SIMS profile of the heterostructure for the top three active layers: the GeSi spacer, the strained Ge quantum well, and the bottom GeSi buffer layer. (d) The RSM of the heterostructure obtained from x-ray diffraction.

profile and the RSM from x-ray diffraction show a Ge quantum well pseudomorphically grown on top of a relaxed $\text{Ge}_{0.73}\text{Si}_{0.27}$ barrier. The details of the growth can be found in Refs. 23, 34, and 35. The heterostructure was not intentionally doped during growth, and no residual 2D holes were measurable in the starting material in low-temperature transport experiments.

In Fig. 2(a), we show the depth profiles of implanted Ga ions at 40 KeV obtained from SRIM/TRIM simulations. Only one normalized profile in the unit of (cm^{-3} per cm^{-3}) was obtained from the simulations. The four curves were scaled from the same curve based on the implantation fluences used in the actual experiment: 8, 12, 16, and $20 \times 10^{11} \text{ cm}^{-2}$ for samples 1, 2, 3, and 4, respectively. At such fluences, the peak Ga densities in the top GeSi barrier layer are between 2 and $5 \times 10^{17} \text{ cm}^{-3}$, much lower than the metal-insulator transition threshold of $\sim 5 \times 10^{18} \text{ cm}^{-3}$ for p-type silicon.³⁶ We expect the threshold density to be comparable in GeSi and, therefore, no metallic conduction in the Ga-doped GeSi barrier layers with a doping density in the low 10^{17} cm^{-3} range even if all Ga dopants are electrically active. The tail of the Ga implant into the Ge quantum well is on the order of 10^{16} cm^{-3} , which translates to an in-well doping level on the order of 10^{10} cm^{-2} . This is a 2D density below the conduction threshold in a Ge quantum well. Figure 2(b) shows a schematic drawing of the valence band diagram in the presence of implanted Ga ions, bulk defect states introduced by implantation damage, and the inevitable surface states. The holes introduced by the implanted Ga ions transfer to three lower-energy states: the bulk defects, the surface states, and the Ge quantum well, in addition to remaining on the Ga ions. Only the holes that transfer to the Ge quantum well are electrically active as a 2D channel at cryogenic temperatures and can be measured in magneto-transport.

The device fabrication process is shown in Fig. 2(c). Alignment marks were first created using photolithography and reactive ion etching. The active channel regions were then defined using photolithography. Only the exposed Hall bar regions were implanted with

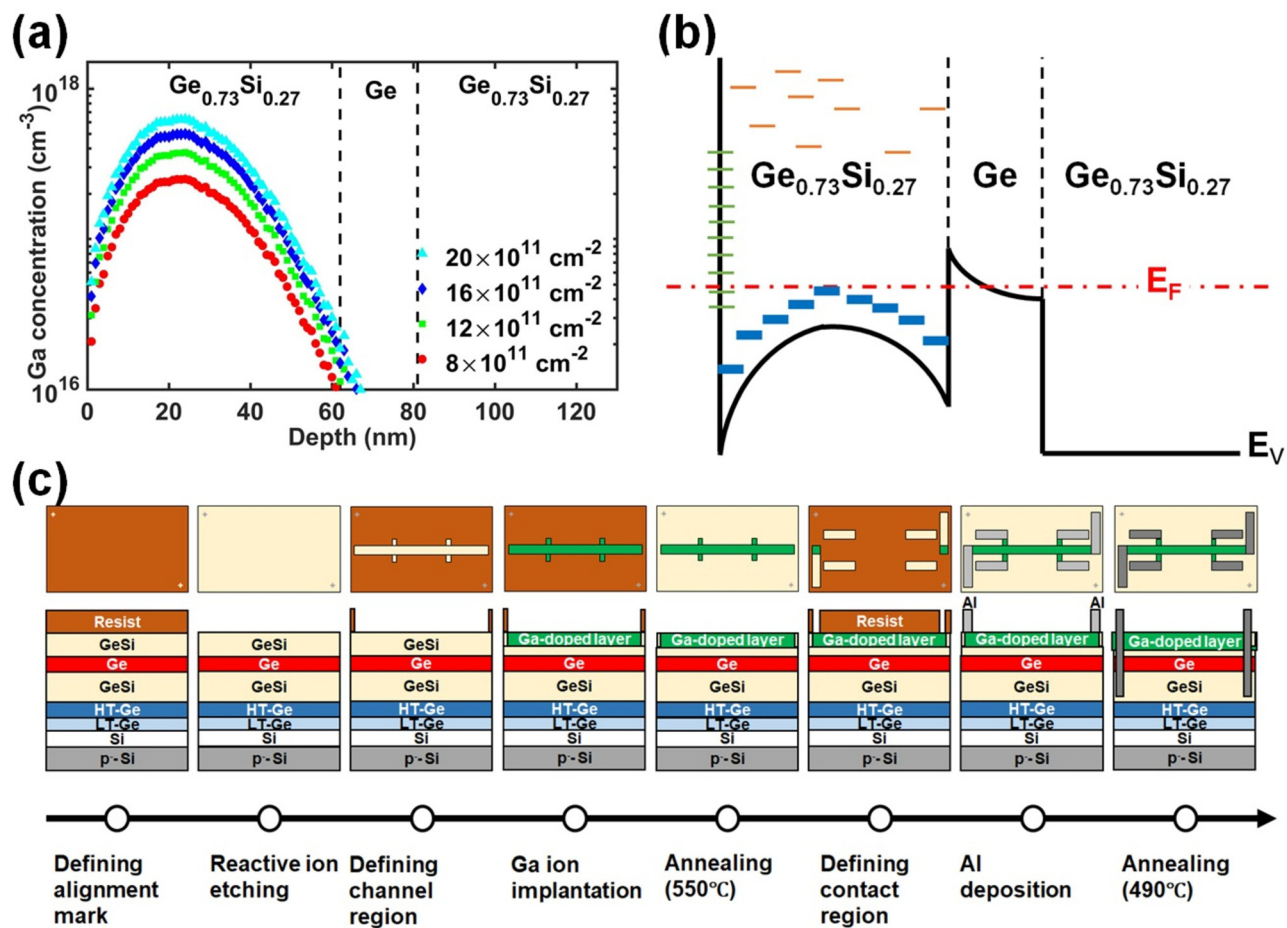


FIG. 2. (a) Simulated distributions of Ga ions in the Ge/GeSi heterostructure implanted at 40 KeV. (b) A Schematic band diagram of the implantation modulation-doped heterostructure. The Ga acceptor states are shown in blue, while bulk defect states are shown in orange and surface states shown in green. (c) The fabrication process flow for making the low-temperature transport testers.

40 KeV Ga ions, while the other regions were protected by photoresist AZ5214. After implantation, the Ga ions were activated in a rapid thermal annealer at 550 °C in a forming gas environment. Electrical contacts were made by depositing Al electrodes and annealing at 490 °C for 30 s in a forming gas environment in a rapid thermal annealer.

Standard lock-in measurements were performed to measure the magnetoresistance in a pumped helium cryostat with a base temperature of 1.1 K. The longitudinal and transverse magnetoresistances (R_{xx} and R_{xy}) are shown in Figs. 3(a)–3(d). The extracted densities for samples 1–4 are 1.3, 2.5, 4.4, and $6.2 \times 10^{11} \text{ cm}^{-2}$. In all samples, we observe clear quantum oscillations in R_{xx} and concomitant plateaus in R_{xy} . The plateaus in R_{xy} are quantized at values consistent with the density extracted from the oscillations in R_{xx} . In sample 1, R_{xx} is vanishingly small at a filling factor of $\nu = 1$, with two oscillations at $\nu = 2$ and 3 visible. As the density increases from sample 1 to sample 4, more and more oscillations become resolved. The resistance minima for the higher density samples (samples 3 and 4) occur only at even filling factors in this magnetic field range, indicating a small Zeeman splitting compared to the cyclotron gap, which is consistent with our

previous observations at high densities.³⁷ We have also carefully measured the temperature dependence of the quantum oscillations for samples 3 and 4 and the weak localization structures for all samples. The data and the details of the analyses are presented in the [supplementary material](#). We obtained an effective mass of $\sim 0.09 m_0$ for sample 3 and $\sim 0.11 m_0$ for sample 4. These extracted values are consistent with previous measurements using undoped HFETs.^{38,39} The increased effective mass at the higher density is attributed to the complex, nonparabolic band structure of the valence band of strained Ge quantum wells.³⁹ In all samples, we only observed weak localization near zero magnetic field. The dephasing rates are approximately linear in temperature, indicating small-angle electron-electron, or in our material, hole-hole, scattering is likely the dominant dephasing mechanism.^{40,41} In short, these observations indicate that the Ga implantation has created a high-quality 2D hole system in the host Ge/GeSi heterostructure, with the density controlled through the implant fluence.

In Fig. 3(e), the 2D hole density is plotted against the Ga implantation fluence, together with a linear fit shown as a blue dashed line.

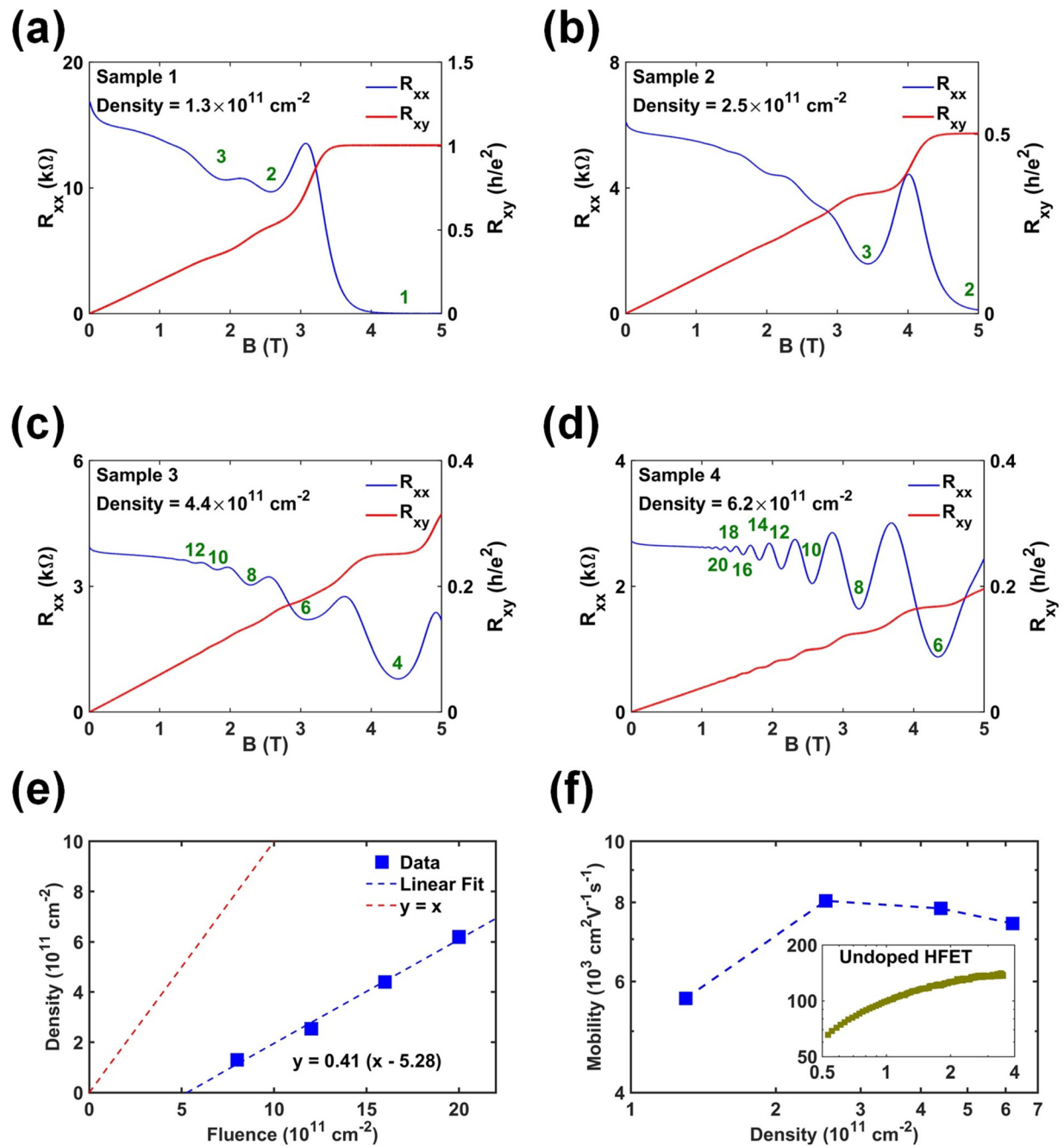


FIG. 3. (a)–(d) Magnetoresistance of the four samples studied in this work at 1.1 K. (e) The measured Hall density vs the Ga implantation fluence. The blue dashed line is a linear fit of the data. The red dashed line is the limit of 100% transfer and 100% activation. (f) Carrier mobility as a function of density of the implanted samples. Inset: mobility vs density for an undoped HFET built using the same material. The units are the same as in the main figure.

The upper limit of 2D hole density would be the implant fluence itself, where every implanted Ga introduces a 2D hole in the quantum well. This situation of 100% electrical activation and 100% charge transfer is shown as a red dashed line. From Fig. 3(e), we can see that the experimentally achieved density is approximately linear in implant fluence.

The data, however, fall below the ideal red dashed line and has a slope of 0.41 and an intercept with zero carrier density at fluence $= 5.28 \times 10^{11} \text{ cm}^{-2}$. The less-than-unity slope arises from less-than-complete electrical activation and partial charge transfer. Some of the holes would transfer to the surface to fill surface states above the Fermi

energy, and some would be trapped by bulk defect states created during ion implantation. In a small energy window, we can approximate the densities of states of the surface and bulk defects as constants. This approximation and the constant density of states of the 2D hole system lead to an approximately linear dependence between the 2D hole density and the implant fluence. The finite intercept indicates that some deeper states need to be filled first before the Fermi energy can be brought near the valence band maximum of the Ge quantum well. These deeper states are likely surface states near the mid gap.^{42–44}

The carrier mobility is plotted against the carrier density in Fig. 3(f) for the four implanted samples. In the inset, we show the mobility-density plot obtained from an undoped HFET built using the same material. We note that the units in the main plot and in the inset are the same. One apparent observation is the much reduced mobility in the implanted samples compared to that in the HFET. In the density range where the two datasets overlap, the mobility is approximately 20 times smaller in the implanted samples. This reduction in mobility is anticipated from the implanted ions in the modulation-doping layer and in the quantum well as well as the damage induced by the implantation, in spite of the partial lattice recovery from thermal anneals. The maximum achievable mobilities in the presence of remote ionized impurities and uniform background charge can be estimated using the Ga depth profiles from SRIM/TRIM simulations shown in Fig. 2(a) and the closed-form expressions in Ref. 45, respectively. Even for the worst-case scenarios – assuming that the dopant densities are at the peak values throughout the modulation-doping layer and the quantum wells – we obtain $\sim 1 \times 10^6 \text{ cm}^2 \text{ V}^{-1} \text{ s}^{-1}$ and $\sim 5 \times 10^4 \text{ cm}^2 \text{ V}^{-1} \text{ s}^{-1}$ for remote ionized impurity scattering and uniform background charge scattering, respectively. Both limits are much higher than the observed mobility, indicating that damage induced during implantation is likely the main limiting factor. We expect that shallower implantation or deeper quantum wells can further spatially separate the 2D system from the damaged regions and improve the mobility. One advantage of the implantation method is that the achievable density is much higher. In the undoped HFET, the density saturates at approximately $3.5 \times 10^{11} \text{ cm}^{-2}$. This saturation behavior is well understood and is due to carriers tunneling from the quantum well to the oxide/semiconductor interface, which becomes a triangular quantum well with an energy lower than the quantum well at high gate biases.^{34,46,47} In modulation-doped structures, the electric field is countered by the ionized dopant cores—Ga ions in our case—and does not create a second lower energy quantum well near the surface even at high densities. As such, when the same heterostructure is used, the upper limit of the 2D hole density in the modulation-doping architecture can be much higher. The estimated peak Ga doping densities in the GeSi barrier layer in our samples, as shown in Fig. 2, are much lower than this conduction threshold in the GeSi layer, which is expected to occur around $5 \times 10^{18} \text{ cm}^{-3}$.³⁶ We, therefore, expect the 2D density to be limited by the high electric field established between the 2D holes and the ionized dopants, which eventually brings the dopant energy lower than the quantum well, preventing further charge transfer. This limiting mechanism is qualitatively similar to that for the undoped HFET, except that here the lower energy states are located at the implanted ions themselves.

We believe that the results presented in this work open up opportunities in nanoscale device design and fabrication. For example, one common failure mode of quantum dot devices based on the undoped

HFETs is leakage from the nanoscale gates to the substrates and between the nanoscale gates. Another issue is the extremely tight packing of the gates at multiple layers. Using ion implantation to create the reservoirs and in-plane finger gates alleviates the gate leakage issue by avoiding a direct overlap between an accumulation gate and a depletion gate and the packing issue by moving some gates to the quantum well level. The distinguishing advantage of the implantation modulation-doping method is selective area doping and local control of the doping type, depth, and density. This freedom enables experiments where electrons and holes can coexist at the nanoscale with controlled depths and densities, which is, otherwise, difficult to achieve. Additionally, in our study, no metallic gates existed on the samples. Yet, the structures contained high-mobility 2D carriers only where they were defined by photolithography. When the method is combined with nanolithography or direct-write nano-implantation,^{48,49} it is conceivable that one can create structures with high-mobility 2D carriers with nanoscale resolution without using metal gates. These implanted modulation-doped nanostructures are easily accessed by microwave or optical probes, enabling experiments difficult to implement using conventional gated devices.

In summary, we have presented a method of achieving post-growth modulation doping by ion implantation. The 2D carrier density can be controlled by the ion implantation energy and fluence. An empirical relation between the 2D hole density and the Ga ion fluence was obtained for an undoped Ge/GeSi heterostructure. It was shown that the implantation creates damage in the structure that could degrade the mobility. Nevertheless, the resulting 2D hole system can be of high quality, as evidenced by the magneto-transport data. One unique advantage of the implantation method is a much wider accessible density range for a given undoped heterostructure. We believe that the presented implantation modulation-doping technique can enable nanostructures and experiments that were previously difficult to create and perform.

See the [supplementary material](#) for extraction of the temperature-dependent magnetoresistance, the effective masses, and dephasing rates of 2D holes in these implantation modulation-doped materials and comparison of the results with the values obtained from gated, unimplanted devices.

We thank Boris Narozhny and Addamane Sadvikas for helpful discussions. This work was funded by the Laboratory Directed Research and Development Program at Sandia National Laboratories (SNL) and by the U.S. Department of Energy (DOE), Office of Basic Energy Sciences (BESs). SNL is a multimission laboratory managed and operated by National Technology and Engineering Solutions of Sandia LLC, a wholly owned subsidiary of Honeywell International Inc. for the U.S. DOE's National Nuclear Security Administration under Contract No. DE-NA0003525. This work was performed, in part, at the Center for Integrated Nanotechnologies, a U.S. DOE, Office of BESs, user facility. This work at National Taiwan University (NTU) was supported by the Ministry of Science and Technology (No. 107-2112-M-002-014) and the Ministry of Education (No. NTU-109L891602). This paper describes objective technical results and analysis. Any subjective views or opinions that might be expressed in the paper do not

necessarily represent the views of the U.S. DOE or the United States Government.

DATA AVAILABILITY

The data that support the findings of this study are available from the corresponding author upon reasonable request.

REFERENCES

- ¹T. Ando, A. B. Fowler, and F. Stern, *Rev. Mod. Phys.* **54**, 437 (1982).
- ²D. P. DiVincenzo, *Fortschr. Phys.* **48**, 771 (2000).
- ³C. Kloeffer and D. Loss, *Annu. Rev. Condens. Matter Phys.* **4**, 51 (2013).
- ⁴A. Hirohata and K. Takanashi, *J. Phys. D: Appl. Phys.* **47**, 193001 (2014).
- ⁵T. Zhou, N. Mohanta, J. E. Han, A. Matos-Abiad, and I. Žutić, *Phys. Rev. B* **99**, 134505 (2019).
- ⁶C. H. Yang, R. C. C. Leon, J. C. Hwang, A. Saraiva, T. Tantt, W. Hwang, J. C. Lemyre, K. W. Chan, K. Y. Tan, F. E. Hudson, K. M. Itoh, A. Morello, M. Pioro-Ladrière, A. Laucht, and A. S. Dzurak, *Nature* **580**, 350 (2020).
- ⁷N. W. Hendrickx, D. P. Franke, A. Sammak, G. Scappucci, and M. Veldhorst, *Nature* **577**, 487 (2020).
- ⁸H. P. Wei, D. C. Tsui, and M. Razeghi, *Appl. Phys. Lett.* **45**, 666 (1984).
- ⁹M. I. Nathan, *Solid State Electron.* **29**, 167 (1986).
- ¹⁰R. Fletcher, E. Zaremba, M. D'Iorio, C. T. Foxon, and J. J. Harris, *Phys. Rev. B* **41**, 10649 (1990).
- ¹¹J. Z. Li, J. Y. Lin, H. X. Jiang, M. Asif Khan, and Q. Chen, *J. Appl. Phys.* **82**, 1227 (1997).
- ¹²O. Ambacher, J. Smart, J. R. Shealy, N. G. Weimann, K. Chu, M. Murphy, W. J. Schaff, L. F. Eastman, R. Dimitrov, L. Wittmer, and M. Stutzmann, *J. Appl. Phys.* **85**, 3222 (1999).
- ¹³O. Ambacher, B. Foutz, J. Smart, J. R. Shealy, N. G. Weimann, K. Chu, M. Murphy, A. J. Sierakowski, W. J. Schaff, L. F. Eastman, R. Dimitrov, A. Mitchell, and M. Stutzmann, *J. Appl. Phys.* **87**, 334 (2000).
- ¹⁴M. Yano, K. Hashimoto, K. Fujimoto, K. Koike, S. Sasa, M. Inoue, Y. Uetsuji, T. Ohnishi, and K. Inaba, *J. Cryst. Growth* **301–302**, 353 (2007).
- ¹⁵H. Tampo, H. Shibata, K. Maejima, A. Yamada, K. Matsubara, P. Fons, S. Kashiwaya, S. Niki, Y. Chiba, T. Wakamatsu, and H. Kanie, *Appl. Phys. Lett.* **93**, 202104 (2008).
- ¹⁶J. Betancourt, J. J. Saavedra-Arias, J. D. Burton, Y. Ishikawa, E. Y. Tsybal, and J. P. Velev, *Phys. Rev. B* **88**, 085418 (2013).
- ¹⁷S. B. Cho and R. Mishra, *Appl. Phys. Lett.* **112**, 162101 (2018).
- ¹⁸T. Lu, J. Liu, J. Kim, K. Lai, D. Tsui, and Y. Xie, *Appl. Phys. Lett.* **90**, 182114 (2007).
- ¹⁹T. Lu, D. Tsui, C.-H. Lee, and C. Liu, *Appl. Phys. Lett.* **94**, 182102 (2009).
- ²⁰R. Willett, L. Pfeiffer, and K. West, *Appl. Phys. Lett.* **89**, 242107 (2006).
- ²¹T. Lu, D. Luhman, K. Lai, D. Tsui, L. Pfeiffer, and K. West, *Appl. Phys. Lett.* **90**, 112113 (2007).
- ²²J. Chen, D. Wang, O. Klocan, A. Micolich, K. Das Gupta, F. Sfigakis, D. Ritchie, D. Reuter, A. Wieck, and A. Hamilton, *Appl. Phys. Lett.* **100**, 052101 (2012).
- ²³D. Laroche, S.-H. Huang, Y. Chuang, J.-Y. Li, C. W. Liu, and T. M. Lu, *Appl. Phys. Lett.* **108**, 233504 (2016).
- ²⁴N. Hendrickx, D. Franke, A. Sammak, M. Kouwenhoven, D. Sabbagh, L. Yeoh, R. Li, M. Tagliaferri, M. Virgilio, G. Capellini, G. Scappucci, and M. Veldhorst, *Nat. Commun.* **9**, 2835 (2018).
- ²⁵A. Sammak, D. Sabbagh, N. W. Hendrickx, M. Lodari, B. Paquelet Wuetz, A. Tosato, L. Yeoh, M. Bollani, M. Virgilio, M. A. Schubert, P. Zaumseil, G. Capellini, M. Veldhorst, and G. Scappucci, *Adv. Funct. Mater.* **29**, 1807613 (2019).
- ²⁶R. Dingle, H. L. Störmer, A. C. Gossard, and W. Wiegmann, *Appl. Phys. Lett.* **33**, 665 (1978).
- ²⁷P. M. Solomon and H. Morkoc, *IEEE Trans. Electron Devices* **31**, 1015 (1984).
- ²⁸R. People, J. C. Bean, D. V. Lang, A. M. Sergent, H. L. Störmer, K. W. Wecht, R. T. Lynch, and K. Baldwin, *Appl. Phys. Lett.* **45**, 1231 (1984).
- ²⁹T. J. Drummond and I. J. Fritz, *Appl. Phys. Lett.* **47**, 284 (1985).
- ³⁰J. Shen, J. D. Dow, S. Y. Ren, S. Tehrani, and H. Goronkin, *J. Appl. Phys.* **73**, 8313 (1993).
- ³¹O. Aktas, Z. F. Fan, S. N. Mohammad, A. E. Botchkarev, and H. Morkoc, *Appl. Phys. Lett.* **69**, 3872 (1996).
- ³²B. R. Bennett, M. J. Yang, B. V. Shanabrook, J. B. Boos, and D. Park, *Appl. Phys. Lett.* **72**, 1193 (1998).
- ³³J. F. Ziegler, M. D. Ziegler, and J. P. Biersack, *Nucl. Instrum. Methods Phys. Res.* **268**, 1818 (2010).
- ³⁴Y.-H. Su, Y. Chuang, C.-Y. Liu, J.-Y. Li, and T.-M. Lu, *Phys. Rev. Mater.* **1**, 044601 (2017).
- ³⁵Y.-H. Su, K.-Y. Chou, Y. Chuang, T.-M. Lu, and J.-Y. Li, *J. Appl. Phys.* **125**, 235705 (2019).
- ³⁶P. Dai, Y. Zhang, and M. P. Sarachik, *Phys. Rev. B* **45**, 3984 (1992).
- ³⁷T. M. Lu, L. A. Tracy, D. Laroche, S.-H. Huang, Y. Chuang, Y.-H. Su, J.-Y. Li, and C. W. Liu, *Sci. Rep.* **7**, 2468 (2017).
- ³⁸W. J. Hardy, C. T. Harris, Y.-H. Su, Y. Chuang, J. Moussa, L. N. Maurer, J.-Y. Li, T.-M. Lu, and D. R. Luhman, *Nanotechnology* **30**, 215202 (2019).
- ³⁹M. Lodari, A. Tosato, D. Sabbagh, M. A. Schubert, G. Capellini, A. Sammak, M. Veldhorst, and G. Scappucci, *Phys. Rev. B* **100**, 041304 (2019).
- ⁴⁰B. L. Altshuler, A. G. Aronov, and D. E. Khmel'nitsky, *J. Phys. C* **15**, 7367 (1982).
- ⁴¹B. L. Altshuler and A. G. Aronov, in *Modern Problems in Condensed Matter Sciences*, Vol. 10 (Elsevier, 1985), pp. 1–153.
- ⁴²H. Hasegawa and T. Sawada, *IEEE Trans. Electron Devices* **27**, 1055 (1980).
- ⁴³A. Dimoulas, P. Tsipas, A. Sotiropoulos, and E. K. Evangelou, *Appl. Phys. Lett.* **89**, 252110 (2006).
- ⁴⁴Q. Xie, S. Deng, M. Schaeckers, D. Lin, M. Caymax, A. Delabie, X.-P. Qu, Y.-L. Jiang, D. Deduytsche, and C. Detavernier, *Semicond. Sci. Technol.* **27**, 074012 (2012).
- ⁴⁵D. Monroe, Y. Xie, E. Fitzgerald, P. Silverman, and G. Watson, *J. Vac. Sci. Technol., B* **11**, 1731 (1993).
- ⁴⁶T. M. Lu, C.-H. Lee, S.-H. Huang, D. C. Tsui, and C. W. Liu, *Appl. Phys. Lett.* **99**, 153510 (2011).
- ⁴⁷D. Laroche, S.-H. Huang, E. Nielsen, Y. Chuang, J.-Y. Li, C.-W. Liu, and T.-M. Lu, *AIP Adv.* **5**, 107106 (2015).
- ⁴⁸M. Singh, J. L. Pacheco, D. Perry, E. Garratt, G. Ten Eyck, N. C. Bishop, J. R. Wendt, R. P. Manginell, J. Dominguez, T. Pluym, D. R. Luhman, E. Bielejec, M. P. Lilly, and M. S. Carroll, *Appl. Phys. Lett.* **108**, 062101 (2016).
- ⁴⁹J. L. Pacheco, M. Singh, D. L. Perry, J. R. Wendt, G. Ten Eyck, R. P. Manginell, T. Pluym, D. R. Luhman, M. P. Lilly, M. S. Carroll, and E. Bielejec, *Rev. Sci. Instrum.* **88**, 123301 (2017).